Publication Year	2022
Acceptance in OA	2025-02-21T18:57:29Z
Title	The Coma Cluster at LOFAR Frequencies. II. The Halo, Relic, and a New Accretion Relic
Authors	BONAFEDE, Annalisa, BRUNETTI, Gianfranco, Rudnick, L., VAZZA, Franco, Bourdin, H., GIOVANNINI, Gabriele, Shimwell, T. W., Zhang, X., Mazzotta, P., Simionescu, A., Biava, N., Bonnassieux, E., BRIENZA, Marisa, Brüggen, M., Rajpurohit, K., Riseley, C. J., Stuardi, C., Feretti, L., Tasse, C., BOTTEON, Andrea, CARRETTI, Ettore, CASSANO, Rossella, Cuciti, V., DE GASPERIN, Francesco, GASTALDELLO, Fabio, ROSSETTI, Mariachiara, Rottgering, H. J. A., VENTURI, Tiziana, van Weeren, R. J.
Publisher's version (DOI)	10.3847/1538-4357/ac721d
Handle	http://hdl.handle.net/20.500.12386/36138
Journal	THE ASTROPHYSICAL JOURNAL
Volume	933

been computed using the same regions. These plots, shown in Figure 12, show a different radio profile in the three sectors we have considered and show clearly a shallower decline of the radio brightness with respect to the X-ray brightness. In the NW sector, we detect a sharp decline of the radio brightness at ∼1900″ i.e., the location of the radio front (see Section 9). In the NE sector a sharp decline of the radio emission is detected at ∼1400″ (670 kpc). This is due to the presence of the filaments of the radio halo (Figure 3) and to the asymmetry of the halo emission, which is more pronounced toward the W. The radio profile in the SE sector shows, instead, a smooth decline.

To inspect the possible change in the relative radial trend of I_R and I_X, we show in the top panel of Figure 13 the ratio I_R/I_X in logarithmic base-10 scale, for the different sectors (NW, NE, and SW). The trend is similar in the three sectors, with a ratio that is smaller in the central part of the halo and that progressively increases. In the three outermost annuli (approximately at 1600″, i.e., ∼750 kpc) the ratio decreases in the NE and SE sectors. This plot shows that the ratio of the two quantities is not constant throughout the halo, consistent with the results obtained in the point-to-point analysis. In the middle panel of Figure 13, we show the ratio of I_R to I_X^β, using the value of β obtained from the point-to-point analysis ($\beta = 0.76$). If the same value of β were representative of the whole halo, we would expect to see a horizontal line. Instead, the plot shows that a single value of β does not represent the whole halo emission. The change in the slope of β is shown more clearly in the bottom panel of Figure 13, where we plot $I_R/I_X^{\beta_{\rm core}}$, where $\beta_{\rm core} = 0.41$ is the best-fit value obtained from the point-to-point analysis restricted to the halo core.

Hence, we conclude that the I_R–I_X correlation has a slope that changes with the radial distance from the cluster center, being flatter in the halo core (where we find $\beta \sim 0.41$) and steeper in the outer halo (where we find $\beta \sim 0.76$. While the slope in the core seems to remain constant, the ratio I_R–I_X^β, shown in the middle panel of Figure 13, indicates a progressive steepening of the correlation with increasing distance from the cluster center.

6.4. Modeling the $\mathrm{I_R}$–$\mathrm{I_X}$ Correlation and Its Radial Trend

A steepening of the I_R–I_X correlation outside the core is expected as a consequence of the different relative weight of inverse Compton and synchrotron losses in a magnetic field declining with radius. Hence, under some assumptions on the magnetic field profile, we can investigate whether the expected radial drop of magnetic field can be entirely responsible for the steepening of the correlation, or whether additional effects are required. We assume a magnetic field profile scaling with the thermal gas as $B(r) \propto B_0 \cdot n_e(r)^{0.5}$, consistent with Bonafede et al. (2010). Note that in this case the Alfvén velocity in the ICM is constant. The radio emissivity in turbulent re-acceleration models can be expressed as

$$\epsilon_R \propto F\eta_e \frac{B^2}{B^2 + B_{\rm IC}^2}, \tag{5}$$

where η_e is the acceleration efficiency, $B_{\rm IC}$ is the CMB equivalent magnetic field, and F is the turbulent energy flux,

$$F \sim \frac{1}{2}\rho\frac{\sigma_v^3}{L}. \tag{6}$$

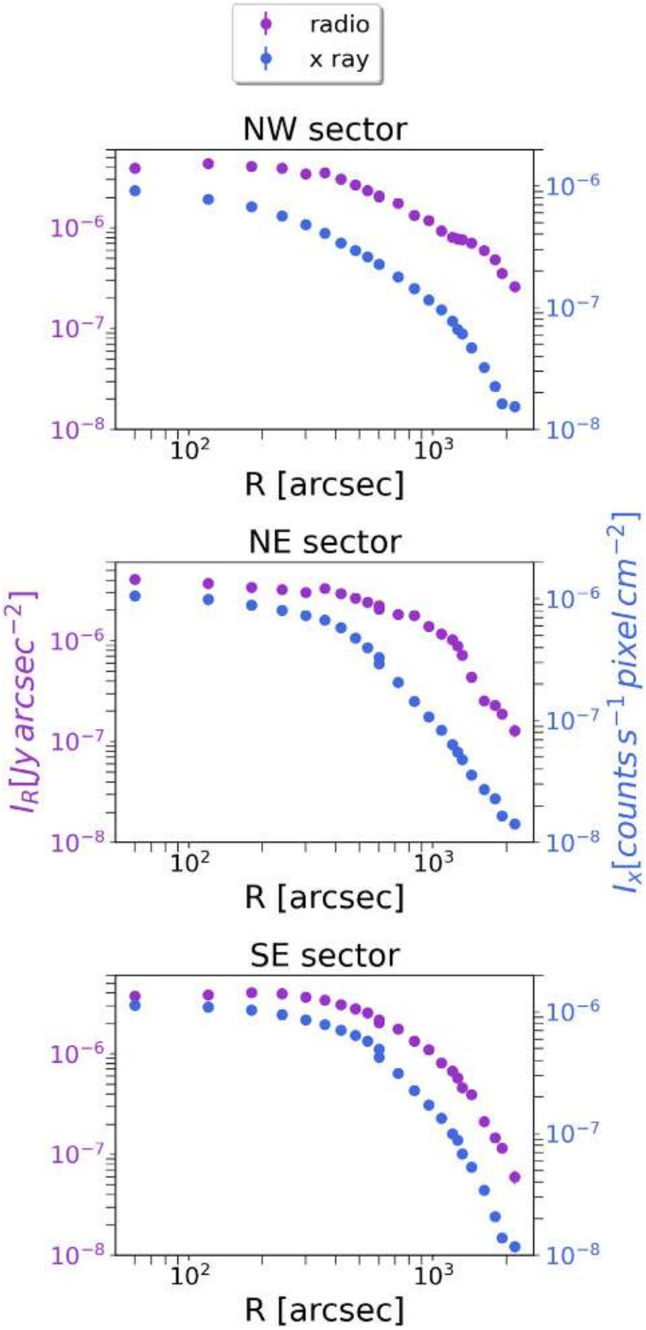

Figure 12. Radial profile of the X-ray brightness and radio brightness in the NW, NE, and SE sectors (top to bottom). The profiles are computed in elliptical annuli with different width from the center to the outermost regions as specified in Figure 8, but excluding the SW sector and dividing the remaining area into three sectors. The outermost annulus in the NW sector shows contamination from soft X-ray protons and has been excluded from the following analysis. Statistical error bars do not appear, as they are smaller than the points.

Here σ_v is the velocity dispersion on scale L, and ρ is the gas density. Assuming an isotropic distribution of electrons in the momentum space, $f(p)$, the acceleration efficiency is (e.g., Brunetti & Lazarian 2007)

$$\eta_e \sim F^{-1}\int d^3p \frac{E}{p^2}\frac{\partial}{\partial p}\left(p^2 D_{pp}\frac{\partial f}{\partial p}\right) \approx \frac{U_{\rm CRE}}{F}(D_{pp}/p^2), \tag{7}$$

where $U_{\rm CRe}$ is the energy density of re-accelerated electrons and D_{pp}/p^2 has different expressions in different re-

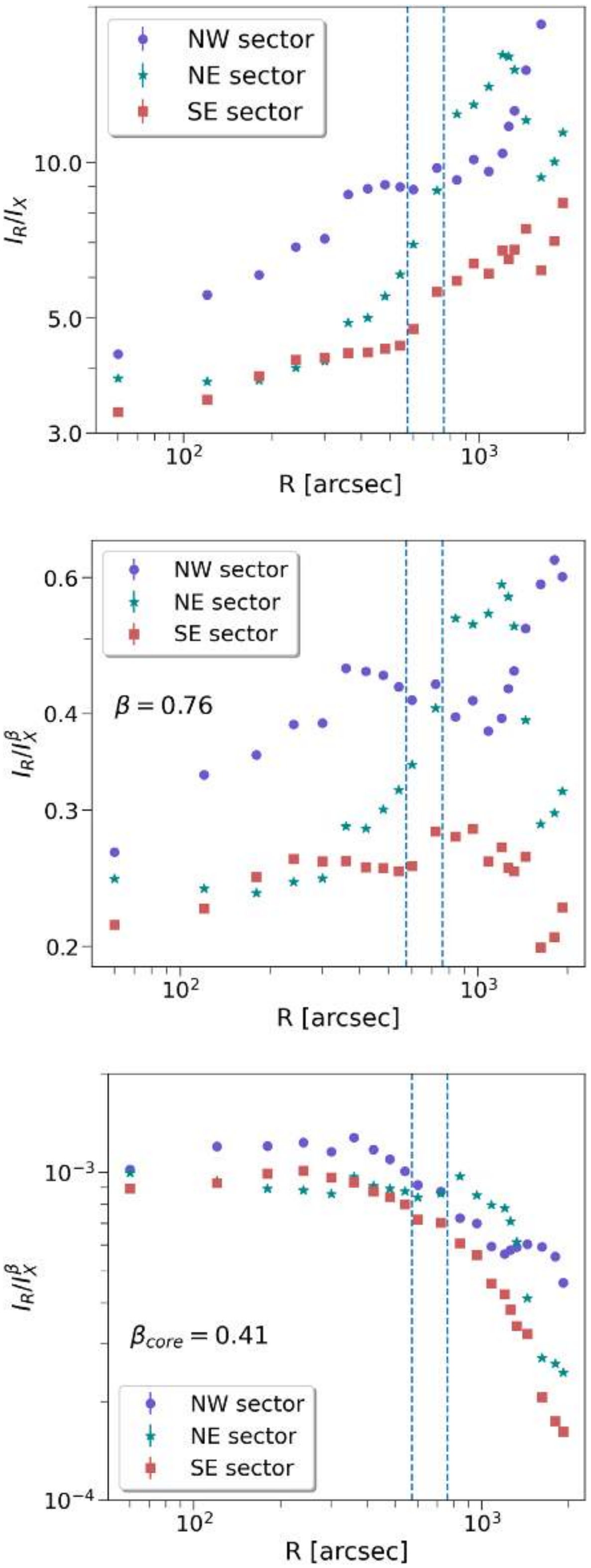

Figure 13. Top: ratio of the radio to X-ray brightness, computed in elliptical annuli as in Figure 12. Middle: ratio of I_R/I_X^β, where $\beta = 0.76$ is the best-fit correlation coefficient found for the whole halo. Bottom: ratio of $I_R/I_X^{\beta_{\rm core}}$, where $\beta_{\rm core} = 0.39$ is the best-fit correlation coefficient found for the halo core. In the three panels, circles, stars, and squares refer to the NW, NE, and SE sector, respectively. Vertical dashed lines mark the position of r_1 and r_2, used to separate the halo core from the outer halo. Statistical error bars do not appear, as they are smaller than the points.

acceleration models. Specifically,

$$\frac{D_{pp}}{p^2} \propto \frac{c_s^2 \mathcal{M}_t^4}{L} \tag{8}$$

in the case of Transit-Time-Damping acceleration with compressive modes (Brunetti & Lazarian 2007; Miniati & Beresnyak 2015) and

$$\frac{D_{pp}}{p^2} \propto \frac{c_s^3 \mathcal{M}_t^3}{L v_A} \tag{9}$$

in the case of non-resonant second-order Fermi acceleration with solenoidal modes (Brunetti & Lazarian 2016). If we also assume a constant temperature and a scenario based on a constant turbulent Mach number, the synchrotron emissivity is

$$\epsilon_R(r) = \epsilon_R(0) \frac{X(r)}{X(0)} \left(\frac{\epsilon_X(r)}{\epsilon_X(0)}\right)^{\frac{1}{2}} \frac{1 + \left(\frac{B_{\rm IC}}{B_0}\right)^2}{1 + \left(\frac{B_{\rm IC}}{B(r)}\right)^2 \left(\frac{\epsilon_X(0)}{\epsilon_X(r)}\right)^{\frac{1}{2}}}, \tag{10}$$

where $\epsilon_X \propto n^2$ is the X-ray (bremsstrahlung) emissivity and $X = \frac{U_{\rm CRE}}{U_{\rm th}}$ the ratio of the energy density of CRe to thermal gas. From the radio and X-ray emissivity, we have computed the projected radio brightness assuming constant X and different values of the central magnetic field, B_0, ranging from 3 to 10 μG and the X-ray brightness using the parameters obtained by Briel et al. (2001). Then, we have computed the slope of the correlation $I_X - I_R$ as a function of the radial distance from the cluster center. The trend of β versus the radial distance is shown in Figure 14 for different values of B_0. We have overplotted as shaded areas the values obtained in the halo core and in the outer halo.

Although all the models predict a steepening of the radio–X-ray scaling with radius, none of them are able to reproduce all observed values. In particular, except for the profile with $B_0 = 5\ \mu$G, the magnetic field profiles that would be compatible with the value of β in the outer halo are higher than those derived from RM studies (Bonafede et al. 2010). Although the central magnetic field derived from RM studies relies on several assumptions, models with a central magnetic field larger than $B_0 > 7/\mu$G were unable to reproduce the observed trend of RM and RM dispersion ($\sigma_{\rm RM}$). Hence, we discard the possibility of $B_0 > 10\ \mu$G to account for the discrepancy between observations and expectations in Figure 14. More likely, a possible scenario to explain the observed trend is to assume that the ratio of the CRe to thermal gas energy densities (X) increases with radial distance from the cluster center. This is indeed expected, as the lifetime of CRe in the ICM increases with the distance from the cluster center owing to the lower Coulomb and synchrotron losses. However, it is the first time that a radially decreasing X seems to be suggested by observational data.

As for the calculations done in Section 5.3.1, we stress that the calculations outlined here are subject to several assumptions and the decrease of X with the distance from the cluster center is only one of the possible causes of the observed I_R–I_X slope.

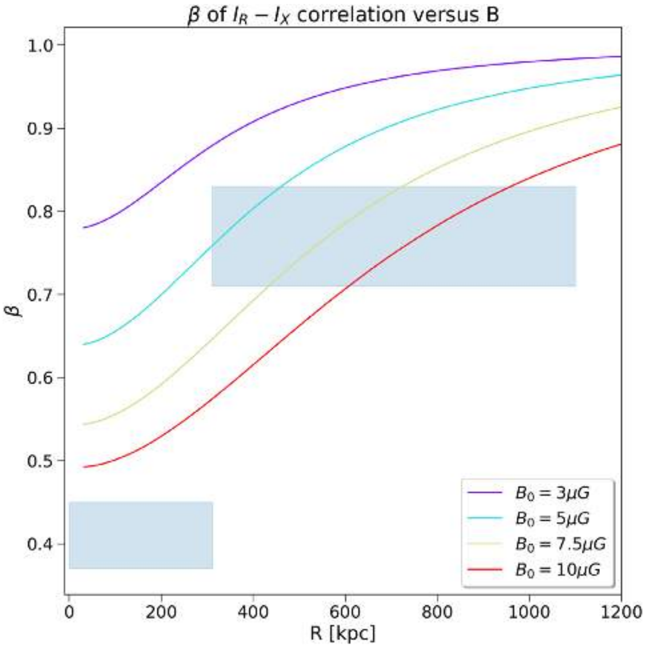

Figure 14. Trend of the radio–X-ray correlation slope β ($I_R = I_X^{\beta}$) with radial distance from the cluster center. β is computed as the ratio of the logarithm of the theoretical projected radio emissivity to the logarithm of the X-ray projected emissivity. The radio emissivity is computed for different values of the central magnetic field B_0, from 3 (top curve) to 10 μG (bottom curve), as specified in the legend. The shaded area refers to the best-fit β obtained from data.

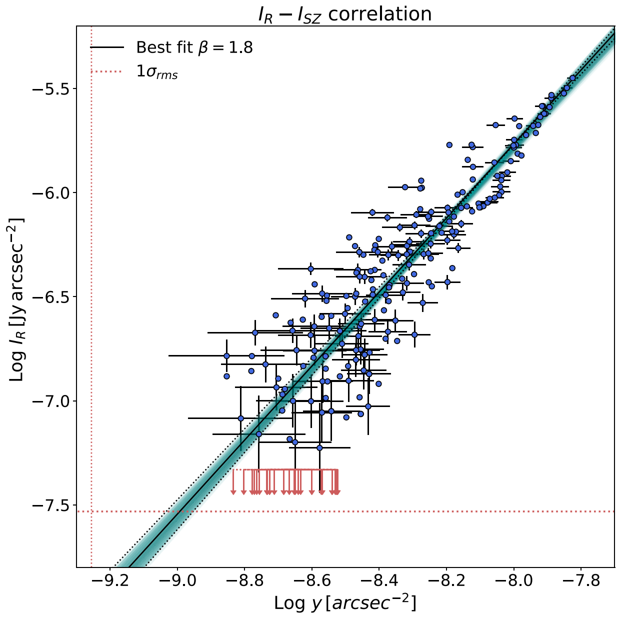

Figure 15. Radio–SZ correlation for the radio halo. The radio image has been convolved to a resolution of 5′, and the source NGC 4839 has been masked. The error bars refer to the statistical errors of the two quantities. Arrows mark the $2\sigma_{\rm rms}$ upper limits. The vertical and horizontal dotted lines mark $1\sigma_{\rm rms}$ for the y-parameter and radio image, respectively. Error bars are plotted every second value.

7. Radio–Thermal Pressure Correlation in the Radio Halo

Resolved SZ maps of the Coma cluster (Planck Collaboration et al. 2013) can be used to understand the connection between the thermal gas and the radio emission. Since the Comptonization parameter y is proportional to the gas pressure integrated along the line of sight ($y \propto n_e T$), it is less contaminated by cold gas clumps with respect to X-ray emission. We have computed the $I_{\rm SZ}$–I_R point-to-point correlation, following the same approach as described above for the I_R–I_X correlation. We have used the radio image convolved to 5′ resolution, to match the y-map resolution.

Initially, we have fit $I_{\rm SZ}$ versus I_R in the same region as the one considered in the I_R–I_X correlation, finding a superlinear slope $\beta_{\rm SZ} = 1.76 \pm 0.08$. Assuming an isothermal model, one would expect that the value found from the $I_{\rm SZ}$–I_R correlation would be twice the scaling of the I_R–I_X correlation. Hence, given the values found from the I_R–I_X correlation, one would expect $\beta_{\rm SZ} = 1.4$–1.6. There is a small tension between SZ and X-ray, which could be due, e.g., to dense and cold X-ray clumps in regions of low surface brightness emission. Understanding the details of this small tension is beyond the scope of this work; what is relevant for our analysis is that regions of high non-thermal energy are regions of high thermal energy, as probed by the $I_{\rm SZ}$–I_R correlation.

The y-map is more extended than the XMM-Newton mosaic and covers regions at the cluster outskirts, where we have a radio halo detection. Hence, we can use the y-parameter map to investigate the correlation between thermal and non-thermal regions up to larger radii from the cluster center, though we miss the resolution given by X-ray data. We have fitted $I_{\rm SZ}$ versus I_R out to a distance of ~1.3 Mpc (~2800″ radius) from the cluster center, which is the maximum distance where we have detected the radio halo. As shown in Section 6, we have an indication from the X-ray analysis that the slope would further increase when outer regions of the halo are considered. We find $\beta = 1.78 \pm 0.08$, which is slightly steeper than the slope found in the inner 2400″ radius, though consistent within the errors. The $I_{\rm SZ}$–I_R correlation is shown in Figure 15. Both X-ray and SZ analyses show that when outer regions of the halo are considered, the correlation slope increases, i.e., the outermost regions of the radio halo have a different ratio of thermal/non-thermal energy than the inner ones.

A correlation between the radio emission and the y-signal has been first obtained by Planck Collaboration et al. (2013), who fitted $I_{\rm SZ}$ versus I_R, finding a quasi-linear relation: $I_{\rm SZ} \propto I_R^{0.92\pm0.04}$, which would correspond to our $\beta \sim 1.1$. They used the WSRT 325 MHz map and y images at 10′ resolution and extracted the radio and y-signal from $r < 50'$ region. As we find a steeper slope, using a lower-frequency radio image, we investigate in the following the possible causes of the different trend. First of all, we are looking at the $I_R - I_{\rm SZ}$ correlation using a radio image at a different frequency than used in Planck Collaboration et al. (2013). In addition, we are able to perform a more accurate subtraction of the contaminating sources, as the highest LOFAR resolution is 6″, and we are less affected by calibration artifacts than the WSRT image. Residuals from contaminating sources would increase the values of the radio brightness in each box, and this effect could be more prominent for boxes at the halo periphery. In this case, the effect would be a flattening of the correlation. The data we have at the moment of writing do not allow us to exclude that this is the cause of the different slope found with LOFAR and WSRT. However, we note that a higher value of the correlation slope for the I_R–I_X at lower frequencies has recently been found by Rajpurohit et al. (submitted) in the halo of the cluster A2256 and by Hoang et al. (2021) in the halo of CIG 0217+70.

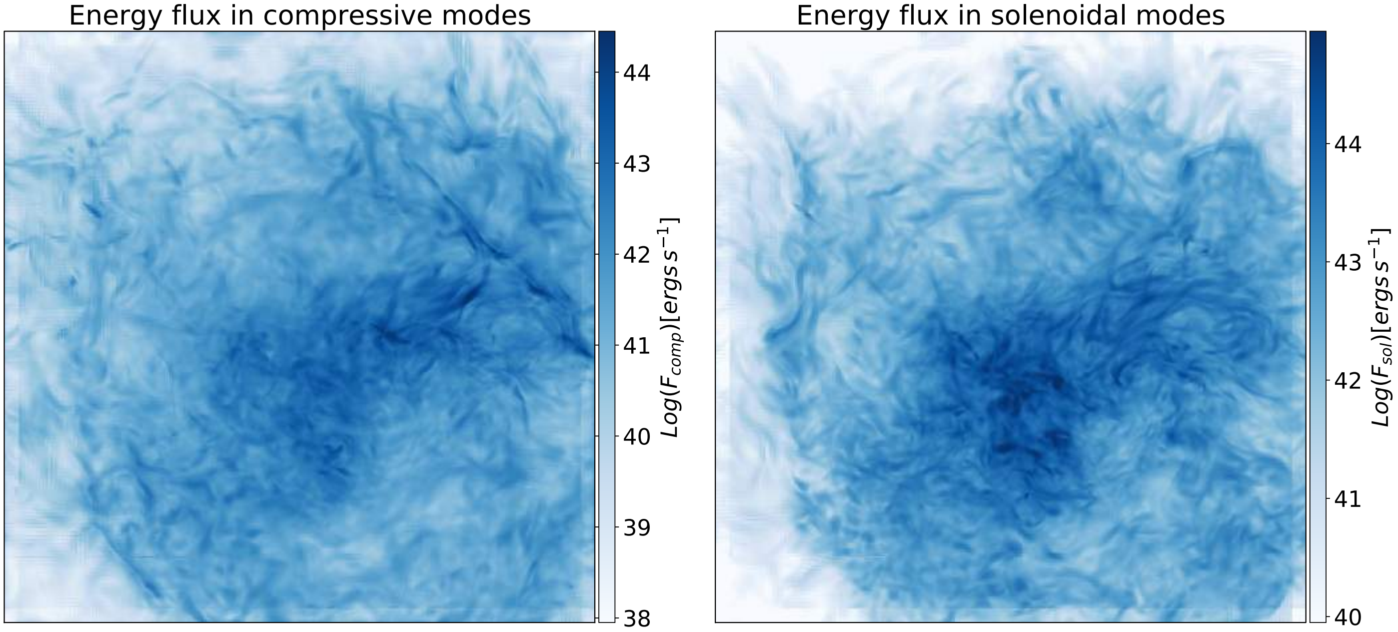

Figure 16. Projected $F_{\rm comp}$ (left) and $F_{\rm sol}$ (right) from MHD cosmological simulations of a Coma-like cluster, from Vazza et al. (2018). Each map has a size of 2560 kpc.

8. Comparison with Numerical Simulations

Having the radio halo resolved in great detail, we can try to understand its origin with the help of numerical simulations. Specifically, we try in this Section to understand whether the observed scaling I_R–I_X can provide useful information to better constrain the particle acceleration mechanism.

8.1. Simulated Thermal to Non-thermal Correlations

We use a Coma-like galaxy cluster, simulated at high resolution and with ideal magnetohydrodynamics using the cosmological Eulerian code ENZO (enzo-project.org) by Vazza et al. (2018). This system has a $z \approx 0.02$ total mass comparable with the real Coma Cluster, and it shows a radial decline of the magnetic field compatible with the estimates from RMs (Bonafede et al. 2010; Vazza et al. 2018). The simulation includes eight levels of adaptive mesh refinement (AMR) to increase the spatial and force resolution in most of the innermost cluster volume, down to $\Delta x = 3.95$ kpc per cell. While this simulation assumes an initial volume-filling background of weak magnetic field, $B_0 = 10^{-4}$ μG (comoving) at $z = 40$, the low-redshift properties of the magnetic field are fairly independent of the exact origin scenario, due to the effect of the efficient small-scale dynamo amplification (e.g., Donnert et al. 2009; Vazza et al. 2021). Using the filtering technique described in Vazza et al. (2017), we have computed the turbulent energy flux, $F_{\rm Comp,Sol}$, associated with the compressive and solenoidal velocity components:

$$F_{\rm Comp,Sol} = \rho \frac{\sigma^3_{v_{\rm Comp,Sol}}}{L} \times \frac{B^2}{B^2 + B^2_{\rm IC}}, \tag{11}$$

where, similarly as in Equation (6), $\sigma_{v_{\rm Comp,Sol}}$ is the dispersion of the compressive, solenoidal velocity field on scale L, different for solenoidal and compressive modes. From F, one can compute the simulated synchrotron luminosity (see Equation (5)) as

$$L_{\rm Comp,Sol} = \eta_e F_{\rm Comp,Sol}. \tag{12}$$

The constant $\eta_e \leqslant 1$ gives the dissipation efficiencies for solenoidal and compressive modes into cosmic-ray acceleration, which depend on the complex physics of cosmic-ray acceleration via the Fermi II process (see, e.g., Miniati & Beresnyak 2015; Brunetti & Lazarian 2016; Brunetti & Vazza 2020). However, since in this application to our new LOFAR observations of Coma we are only concerned with the relative distribution of the two energy fluxes, we fix η for simplicity, acknowledging that both fluxes will represent an overestimate (likely by a factor $\geqslant 10^2$) of the effective dissipation onto cosmic-ray acceleration. Hence, we have used $F_{\rm Comp,Sol}$ as a proxy for the synchrotron luminosity instead of $L_{\rm Comp,Sol}$. The maps of projected $F_{\rm Comp}$ and $F_{\rm Sol}$ are shown in Figure 16. We have computed the correlation between $F_{\rm Comp,Sol}$ and the simulated X-ray brightness I_X as we have done for the radio and X-ray emission.

As we want to compare the observed scaling between I_R and I_X with simulated quantities, we have checked that we are not affected by different trends of I_X in the simulation with respect to observations. In Figure 17, we show the X-ray radial profiles obtained from observations and simulations, computed in the energy band 0.5–2 keV. The observed and simulated profiles have been rescaled to better compare the radial trends, that taking errors into account, results are consistent, and hence will not affect the comparison between simulated and observed thermal to non-thermal properties.

We note that some assumptions must be made to compare the simulated $F_{\rm Comp,Sol}$ to the observed radio emission. Specifically, we have assumed that the halo emission is generated by turbulent re-acceleration, and that η_e is constant throughout the cluster volume. Furthermore, as we are not modeling the CRe component, we have averaged $F_{\rm Comp,Sol}$ on scales larger than the electron diffusion length at 144 MHz. The

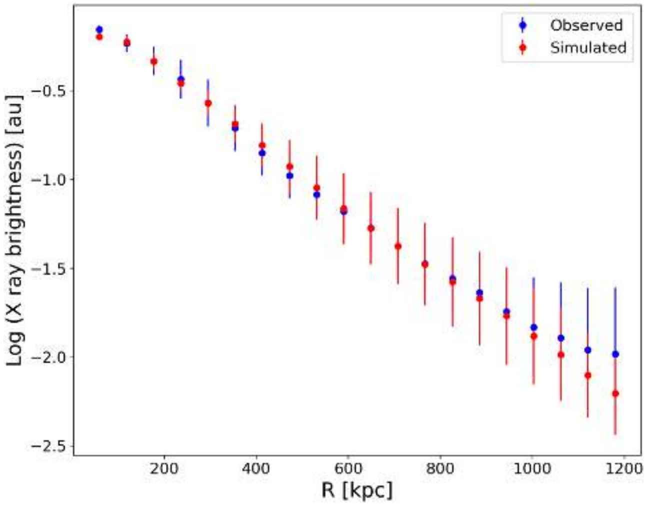

Figure 17. Simulated (red) and observed (blue) radial profiles of the X-ray brightness. The values have been computed in circular annuli. We plot the average (circles) and the standard deviation within each annulus (error bars).

diffusion length l_e of electrons emitting at 144 MHz can be estimated at first order as

$$l_e \sim 2\sqrt{D\tau_{\rm rad}} \sim 100\ {\rm kpc}. \qquad (13)$$

Here $\tau_{\rm rad}$ is the electrons' radiative age at 144 MHz ($\tau_{\rm rad} \approx$ 200 Myr) and D is the spatial diffusion coefficient. A simple estimate for D (i.e., ignoring pitch-angle scattering along magnetic field lines) can be obtained from the typical scale for MHD turbulence in the ICM ($l_A \sim 0.1$–0.5 kpc) as $D \approx \frac{1}{3} l_A c$.

We have computed the mean of $F_{\rm Comp,Sol}$ and I_X in boxes of 160 kpc a side, which is larger than l_e and comparable to the size of the boxes used to compute the I_R–I_X correlation from data (see Section 6).

In Figure 18, the two correlations obtained with simulated data are shown. Both $F_{\rm Comp}$ and $F_{\rm Sol}$ are positively correlated with the simulated I_X. The correlation slope is similar, though a bit steeper in the case of $F_{\rm Sol}$–I_X (see Table 6). Both slopes are consistent with the observed I_R–I_X correlation, supporting the connection between turbulence and radio diffuse emission. We note that the power in the solenoidal energy flux is ∼10% higher than in the compressive energy flux. Once the CRe emission is properly modeled, this could be used to disentangle the role played by the two modes for CRe re-acceleration.

8.2. Correlations in the Center and Peripheral Regions

As shown in the previous section, the global I_R–I_X in the Coma cluster can be recovered using both compressive and solenoidal energy fluxes as a tracer for the radio emission. MHD simulations show that solenoidal modes are dominant in the cluster central regions and compressive modes dominate the cluster outskirts (Miniati & Beresnyak 2015; Vazza et al. 2017). We have seen in Section 6 that the different β obtained in the halo core and in the outer halo cannot be explained by the decline of the magnetic field only. Here we investigate whether different turbulent modes could play a role. We have fitted the simulated $F_{\rm comp,sol}$ versus the simulated X-ray brightness I_X in the cluster core and in the cluster external regions separately. We used boxes of 32 kpc size to have a better sampling of the halo core. The results are listed in Table 6.

The best-fit slopes for the outer halo are consistent with the global slopes. For the halo core alone, which samples a narrow region of $I_X - F_{\rm comp,sol}$ space, the correlation is poor (Pearson correlator coefficient $\rho_{\rm P} = 0.2$–0.3) and shows a formal fit for the slopes that is flatter than the others.

Hence, we conclude that globally the trends are in agreement with the scenario where turbulent re-acceleration produces the radio halo. In order to understand the process in more detail, the CRe distribution needs to be modeled.

8.3. Simulated Radio–SZ Correlation

Here we investigate the correlation between the simulated SZ signal and the values of $F_{\rm comp}$ and $F_{\rm sol}$ that we have considered as proxies for the radio emission. Following the same procedure detailed in the previous sections, we have computed the correlation between $F_{\rm Comp,Sol}$ and the simulated SZ brightness, as we have done for the radio and SZ emission. The $F_{\rm Comp,Sol}$–$y_{\rm sim}$ correlations are shown in Figure 19. We find that the simulated SZ signal ($y_{\rm sim}$) correlates with both $F_{\rm comp}$ and $F_{\rm sol}$. Specifically, we find a superlinear slope $\beta_{\rm SZ} = 1.8 \pm 0.1$ between $F_{\rm comp}$ and $y_{\rm sim}$, with a Pearson correlator coefficient of $\rho_{\rm P} = 0.8$, and a slope $\beta_{SZ} = 1.9^{+0.1}_{-0.1}$ between $F_{\rm sol}$ and $y_{\rm sim}$ (Pearson correlator coefficient $\rho_{\rm P} = 0.8$). These trends are in very good agreement with the observed trend between y and I_R and support the idea that radio halos are powered by turbulence. As already noted for the simulated $I_X - I_R$ correlation, it is possible that once the CRe distribution is properly modeled, the comparison between simulations and observations will yield information to determine which of the turbulent modes are responsible for particle (re)acceleration.

9. The Halo Front

Previous studies pointed out the presence of discontinuities in the thermal gas cluster properties located at the western edge of the radio halo (Markevitch 2010; Planck Collaboration et al. 2013; Simionescu et al. 2013). This discontinuity, detected in both the Comptonization parameter y and the temperature and deprojected density profiles, is consistent with an outwardly propagating shock front, located ∼33′ (910 kpc) from the cluster center. More recently, Churazov et al. (2021) used X-ray data from eROSITA and confirmed the presence of a shock wave in the west, with a Mach number $M \sim 1.5$. This shock is interpreted as a secondary shock, or "mini-accretion shock," driven by the first passage of the NGC 4839 group through the cluster before reaching the apocenter and inverting its orbital motion. According to this scenario, both the relic and the west shock would be caused by the merger of NGC 4839 with the Coma Cluster. During its first passage, NGC 4839 would have driven a first shock that should now be located at the position marked by the radio relic. The gas displaced by the merger would settle back into hydrostatic equilibrium, forming a "mini-accretion" shock. We refer the reader to Burns et al. (1994), Lyskova et al. (2019), Churazov et al. (2021), and Zhang et al. (2021) for a more detailed explanation of the proposed merging scenario.

Our LOFAR image confirms the presence of an edge of the radio halo toward the west (see Figure 4), which could be in line with the scenario explained above. Shocks in the ICM are often associated with radio relics, where they leave a clear imprint on the spectral index distribution. The spectral index profile is flatter where particles are freshly re-accelerated and

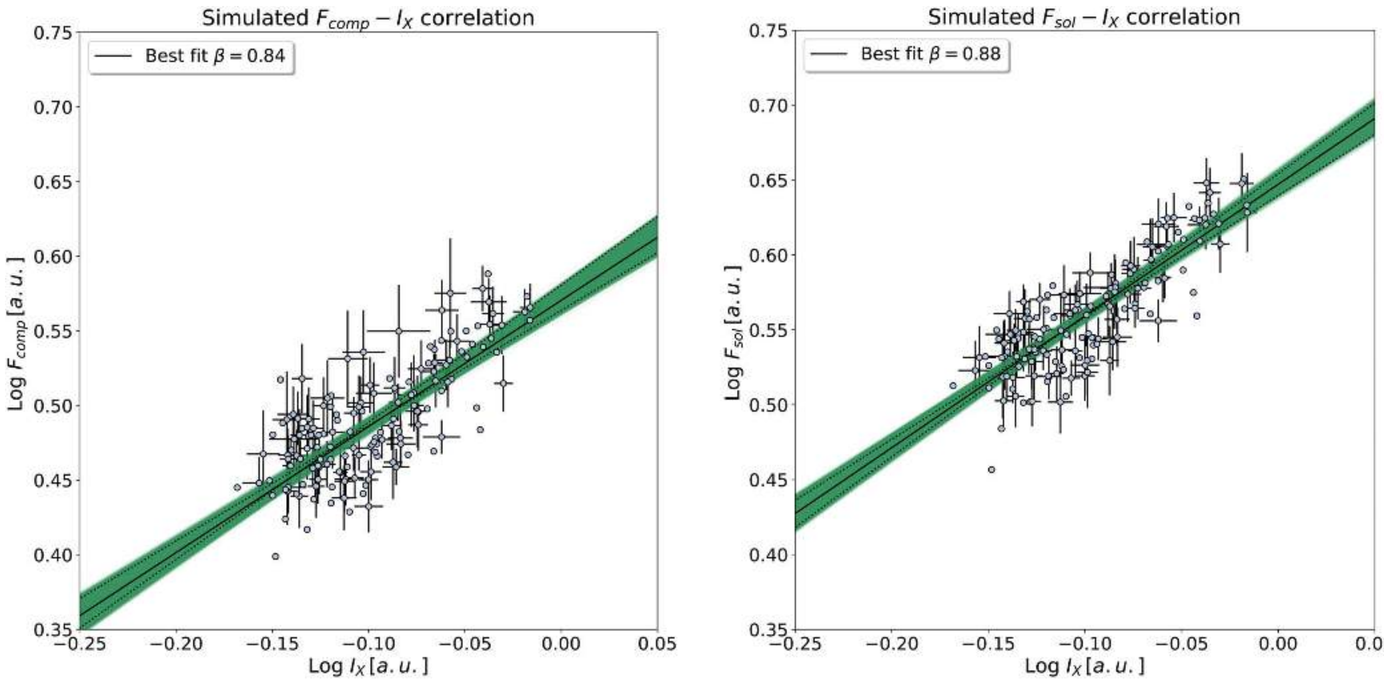

Figure 18. Left panel: F_{Comp}–I_X correlation from simulated data. Right panel: $F_{\mathrm{Sol}} - I_X$ correlation from simulated data.

Table 6
Correlation between Thermal and Non-thermal Simulated Quantities

	β	10%–90%	ρ_{P}
F_{Sol}–I_X	0.88	0.94–0.81	0.8
F_{Comp}–I_X	0.85	0.92–0.77	0.8
	Halo Core		
F_{Sol}–I_X	0.5	0.6–0.4	0.2
F_{Comp}–I_X	0.5	0.6–0.3	0.3
	Outer Halo		
F_{Sol}–I_X	0.83	0.91–0.75	0.8
F_{Comp}–I_X	0.78	0.87–0.69	0.8
F_{Sol}–y_{sim}	1.9	2.0–1.7	0.8
F_{Comp}–y_{sim}	1.8	1.9–1.7	0.8

Note. Column (1): quantities considered in the correlation. Column (2): best-fit slope (median value of the posterior distribution). Column (3): 10th–90th percentiles of the slope posterior distribution. Column (4): Pearson correlation coefficient.

steeper moving toward the downstream region where particles radiate their energy via synchrotron and inverse Compton losses. We have investigated whether a similar trend is found in the "halo front," computing the spectral index profile in annuli that follow the front (Figure 20). To derive the spectral index values, we have used the same images presented in Section 5.[22] In Figure 20, we show the spectral index profile obtained in annuli that follow the front, in comparison with the global spectral index trend obtained in annuli centered on the cluster and excluding the halo front region (Figure 20, left panel). We note that in the direction of the front the spectral index is flatter, but no steepening in the putative downstream region is present. However, the outermost annuli seem to follow a different trend than the global halo profile: the spectral index remains almost constant, while a radial steepening is detected when the whole halo is considered. It is possible that we are limited by the resolution, as the width of the annuli is ∼2′, corresponding to ∼60 kpc, which is larger than the electron cooling length in the post-shock region (e.g., Kang et al. 2012). Hence, it is possible that we do not have the resolution to separate the shock front from the post-shock region, where particles have already experienced strong radiative losses. An alternative scenario is that the radio front could be radio plasma re-accelerated by the same mechanism responsible for the halo emission and then dragged by the shock passage and compressed by it. Possibly, future high-resolution observations at higher or lower frequency will allow us to understand whether the halo front shows the typical shocked spectral index profile that we detect in radio relics or not.

10. The NAT–Relic Connection

The diffuse emission connecting the relic to the NAT radio galaxy NGC 4789 is imaged here with unprecedented resolution, which allows us to detect substructures in its surface brightness distribution. In particular, the bent jets of NGC 4789 do not blend smoothly into the diffuse emission, as observed in other cases of radio galaxies nearby relics (Bonafede et al. 2014; van Weeren et al. 2017; Stuardi et al. 2019), and two discontinuities between the endpoint of the jets and the diffuse emissions are detected. At the center of the diffuse source region, there is a bright transverse bar. Such a bar has been detected in other bent tails (e.g., in A2443, Clarke et al. 2013; and recently in the Shapley supercluster, Venturi et al. 2022) and is predicted by simulations of interacting AGN tails and shocks (Nolting et al. 2019). The length of this source, measured from the relic's edge down to the endpoints of the jets, is 10′, corresponding to 280 kpc at the Coma redshift.

---

[22] We recompute the spectral index radial trend in this section to better highlight the differences between the front region and the rest of the halo, while in Figure 9 we have divided the halo into four identical sectors. For the same reason, the spectral index is computed out to a smaller distance from the cluster center than in Figure 9.

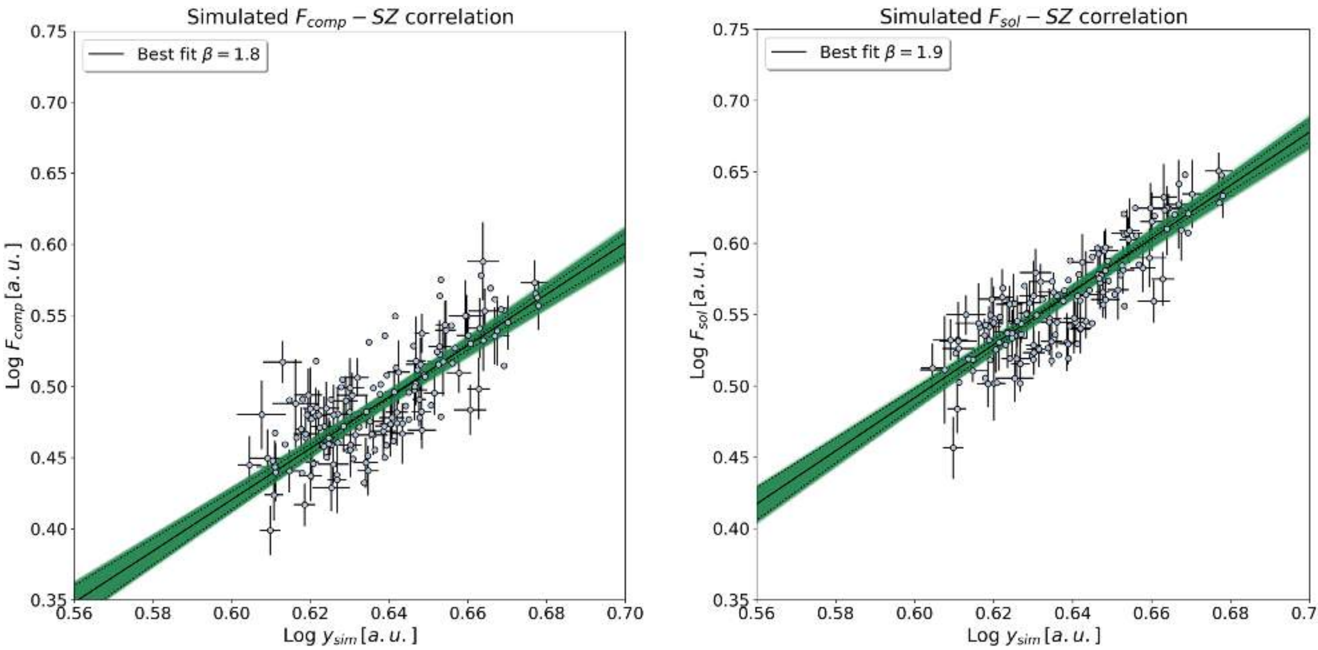

Figure 19. Left panel: $F_{\rm Comp}$–SZ correlation from simulated data. Right panel: $F_{\rm Sol}$ − SZ correlation from simulated data.

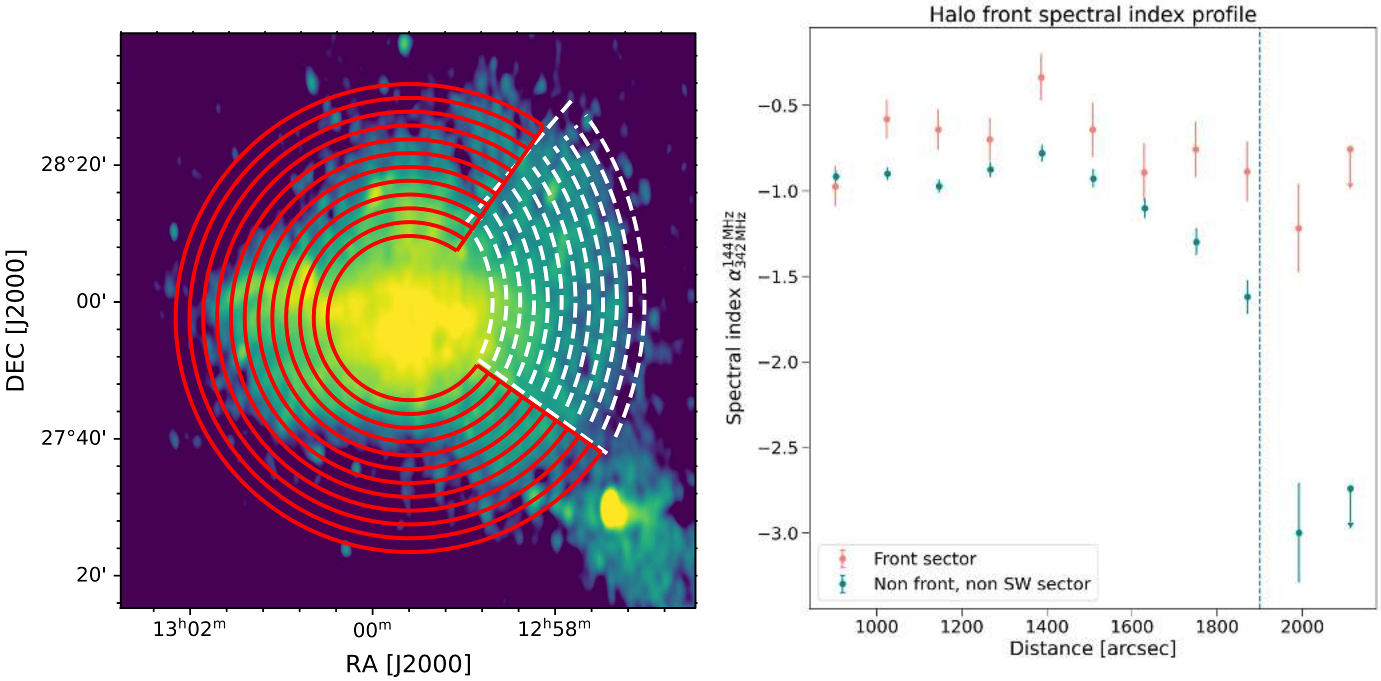

Figure 20. Left panel: annuli used to compute the spectral index trend in the halo front region (white dashed) and in the outer halo (red). Right: spectral index trend computed in the annuli shown in the left panel. Arrows indicate 3σ upper limits. The vertical dashed line indicates the position of the halo front. Error bars only show statistical errors; the values of the spectral index are also affected by the flux calibration uncertainties of WSRT and LOFAR (10% and 15%, respectively), which would contribute with an additional error of 0.2.

To investigate the possible connection of the radio plasma with the thermal gas, we have used the ROSAT image and the radio image at 35″ resolution and investigated the existence of a correlation between the thermal and non-thermal plasma, as done already for the radio halo (see Section 6) and for the Coma bridge (Bonafede et al. 2021).

The average brightness profile of the NAT–relic connection is largely constant, increasing close to the relic edge, where the radio bar is located. In addition, the low counts in the X-ray image do not allow us to make a proper analysis. Hence, though no correlation or anticorrelation between the two quantities seems to be present, no firm conclusions can be derived, and we cannot rule out that the radio emission originates from phenomena similar to those responsible for the bridge. However, given its morphology, we will investigate below an alternative scenario.

The spectral index trend along the NAT–relic connection main axis is shown in Figure 21. We have used the WSRT R image (see Table 2 in Giovannini et al. 1991) that has been used already in Bonafede et al. (2021) to analyze the bridge. Although the higher resolution of the image by Brown & Rudnick (2011) would provide a better description of the spectral index trend, calibration errors from Coma A are strongly affecting that region. The spectrum of the radio emission computed between 144 and 326 MHz shows a gradual steepening from regions close to the AGN core toward the relic's outer edge, reaching values of $\alpha = -1.6 \pm 0.2$. At the relic's outer edge, the spectral index flattens to $\alpha = -1.2 \pm 0.2$, and it steepens toward the NE, i.e., the putative post-shock region, reaching again $\alpha = -1.6 \pm 0.2$. We note that the spectrum starts to flatten already in front of the relic edge (at $\sim 77'$ from the cluster center), though within the error that value is consistent with the steepest point. This apparent flattening could be due to projection effects, as if the relic has a velocity component along the line of sight, some relic emission could appear in front of the relic edge in projection.

Overall, the spectral trend detected along the tail of NCG4789 and in the NAT–relic connection is consistent with AGN particle aging. NGC 4789 would be moving toward the SW of the cluster injecting particles into the ICM. Thus, more recently injected particles are closer to the AGN core than the older ones that have been left behind. The shape of the source and the connection with the radio relic make this source peculiar and suggest a link between the NAT–relic connection and the shock wave that would power the radio relic.

However, according to the merging scenario outlined in several papers (Venturi et al. 1990; Giovannini et al. 1991; Churazov et al. 2021), NGC 4789 would be in the pre-shock region. Hence, it is puzzling to understand how features like the bar could have been formed because that emission has not yet interacted with the shock. Enßlin & Gopal-Krishna (2001) have proposed that the plasma from NGC 4789 is dragged by the infalling matter (falling into Coma's cluster) to the location of the relic, where it is re-energised adiabatically by the shock wave.

Three possible scenarios could in principle explain the emission of the NAT and its connection with the relic, and we briefly outline them here:

1. NGC 4789 is in the pre-shock region, and the shock wave responsible for the relic is moving toward the SW and approaching the tail. In this scenario, the emission from the tail in the NAT–relic connection region would be unaffected by the shock passage. However, the plasma injected into the ICM by the tail would play an important role in explaining the relic emission, as it would furnish energetic electrons that the low Mach number shock wave would reaccelerate.
2. The relic is powered by a quasi-stationary accretion shock, and NGC 4789 is moving supersonically and crossing the shock region from NE to SW. Hence, NGC 4789 would be in the pre-shock region, but its tail would have crossed the shock wave responsible for the relic emission.
3. The relic is powered by a shock wave that is moving toward the cluster center. NGC 4789 has been crossed by the shock, and it is now in the post-shock region.

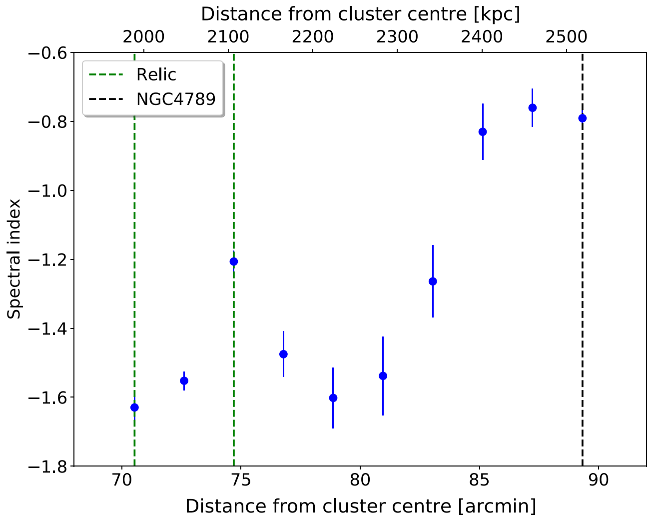

Figure 21. Spectral index profile between 326 and 144 MHz of the emission called the NAT–relic connection. Images at the WSRT resolution $(100'' \times 150'')$ have been used to compute the spectral index in each box.

Scenario (iii) has been recently studied by Nolting et al. (2019) using numerical simulations. They have analyzed the case of a shock wave that crosses an AGN when the shock normal is perpendicular to the jets. They find that when a shock passes through the active jets and lobes of an AGN, jets are distorted by the shock passage, creating an NAT morphology, and a structure similar to the radio bar, as observed here. The spectral index trend resulting from the simulations by Nolting et al. (2019) is in agreement with the one observed here along the tail and NAT–relic connection, though the values are slightly flatter after 200 Myr from the shock passage, when the simulation stops. This scenario would require a shock wave moving toward the cluster center, which seems disfavored by some authors (Feretti et al. 2005; Akamatsu et al. 2013; Churazov et al. 2021) and also by the spectral index trend across the relic that we detect, which is steepening NE, in agreement with expectation from an outward-moving shock wave. In scenario (ii), the situation would have some similarities with the simulation by Nolting et al. (2019), as also in this scenario the AGN would be crossed by a shock. However, in this case, the AGN would be in the pre-shock region, and its tail would be interacting with a less dense environment than the one simulated by Nolting et al. (2019). Scenario (ii) seems also supported by the analysis of Adami et al. (2005), where they detect a relative velocity of ~ 1000 km s^{-1} between NGC 4789 and NGC 4839, at the cluster center. Our analysis does not allow us to discard scenario (i), where the shock is overtaking the preexisting tail from the back. We can see that the tail and shock must be interacting because the tail abruptly stops at the position of the relic. This situation has not been simulated yet, but it is likely that it would require some fine-tuning of the parameters. We indicate scenario (ii) as the favored one, given the data we have now, though it remains to be seen whether the interaction of the AGN tail with a preshocked environment at the cluster outskirts would create the substructures that we observe. In all scenarios, the NAT galaxy NGC 4789 would be providing seed electrons that are (re)accelerated by the shock and originate the radio relic. In the literature, there are a few other cases where a link between an AGN tail and a relic has been established (see Bonafede et al. 2014; van Weeren et al. 2017; Stuardi et al. 2019).

11. Discussion and Conclusions

In this work, we have used new data at 144 MHz from LOFAR to analyze the emission from the Coma cluster. We summarize our findings in the following and discuss how these observations allow us to advance our understanding of the nonthermal emission in clusters of galaxies.

We have focused our analysis on the properties of the radio halo, which—detected at 144 MHz with the resolution and sensitivity allowed by LOFAR—presents new interesting features and allows us to perform detailed resolved studies of the radio emission. We find the following:

1. The radio halo at 144 MHz appears larger than previously reported in the literature, with a largest angular scale of $\sim 71'$, corresponding to $\sim$2 Mpc. The halo is connected to the relic through a low surface brightness radio bridge, and the relic is connected to the AGN NGC 4879 to the SW. In total, the radio emission from the halo to the head of NGC 4879 spans $\sim 2^\circ$, corresponding to $\sim$3.4 Mpc.
2. The halo brightness profile is well fitted by an exponential elliptical profile. At 144 MHz, it is characterized by e-folding radii $r_1 = 355$ kpc and r_2=268 kpc. At 325 MHz, the profile is more peaked, with r_1 =268 kpc and $r_2 = 240$ kpc. This is consistent with a spectral steepening of the radio emission toward the halo outskirts, in agreement with the results by Giovannini et al. (1993). It would be useful to perform these fits also at other frequencies in order to study how the halo size changes with frequency.
3. The spectrum of the radio halo between 144 and 342 MHz is flatter than previously reported, though consistent within the errors. We find $\alpha = -1.0 \pm 0.2$, while previous studies indicate $\alpha \sim -1.2$. We have computed the flux density of the halo at both frequencies from the best-fit exponential model, which is less affected by the different sensitivities of the two images and the possible presence of residuals from unrelated sources.
4. We have computed the radial trend of the spectral index α dividing the halo into four symmetric sectors. Our estimates could still be affected by residual contamination from unrelated source and calibration errors, but these should not have a major impact on the global results. We detect for the first time a moderate steepening toward the cluster center of the spectral index and confirm the steepening toward the cluster outskirt found at higher frequencies by Giovannini et al. (1993). This trend is in agreement with the expectations of homogeneous turbulent re-acceleration models. Though a detailed modeling is needed to understand the effect of projection effects and the exact location of the steepening frequency, we argue that the steepening detected at the cluster outskirts could indicate a non-constant acceleration time and hint at a constant turbulent Mach number. The spectral index steepening toward the cluster center is more or less pronounced in the different sectors, being prominent in the SW sector and not clearly detected in the NE sector. It is possible that the SW sector has been perturbed by the passage of the NGC 4839 group and shows now different properties.
5. The point-to-point analysis between radio and X-ray surface brightness indicates a sublinear slope of nonthermal plasma with respect to the thermal plasma. We obtain $I_R \propto I_X^{0.64}$ when the correlation is computed on images at $1'$ resolution. We detect a steeper, yet sublinear, correlation when the radio image is convolved with Gaussian kernels of $2'$, $3'$, $4'$, $5'$, and $6'$, and it converges to $I_R \propto I_X^{0.76}$. Indeed, images at lower resolution are more sensitive to the weak emission in the halo outermost regions. We note that the total halo flux density does not change when computed from the $35''$ or $6'$ image because the outermost regions of the halo yield a very minor contribution to the total halo flux density. However, these regions affect the radio–X-ray correlation, making it steeper.
6. We have investigated whether the radio–X-ray correlation has a different slope in the halo core than in the outer halo, finding that the correlation is flatter in the core ($I_R \propto I_X^{0.41}$) than in the outer halo ($I_R \propto I_X^{0.76}$). By investigating the radial trend of the quantity I_R–I_X, we have confirmed that this trend can be interpreted as a radial trend of I_R versus I_X being flatter in the halo core. An opposite slope change has been recently found in some cool-core clusters, where the mini halo emission is surrounded by a weaker and more extended component (Biava et al. 2021). A flatter slope in the halo core is inconsistent with a major contribution of secondary electrons produced through hadronic interaction between thermal protons and cosmic-ray protons in the ICM.
7. In the framework of homogeneous re-acceleration models, the change of the slope of the I_R–I_X correlation can be only partially accounted for by a declining magnetic field profile. We have investigated the role of X, i.e., the ratio of CRe to thermal energy density, and find that a radially increasing value of X would provide a better match with data. Although more detailed modeling should be done to derive firm conclusions, we note that an increasing value of X with the distance from the cluster center is also expected from a theoretical point of view.
8. With the help of MHD cosmological simulations, we have computed the turbulent energy flux associated with the compressive and solenoidal velocity components in a Coma-like cluster, and we find that both quantities show a sublinear scaling with the simulated X-ray emission, which is in agreement with the observed scaling of I_R versus I_X. Assuming the same efficiency for both modes, the flux associated with the solenoidal velocity component is a factor 10 higher than the flux associated with the compressive component. Hence, once the CRe distribution throughout the volume is assumed, it would be possible to constrain the relative importance of the two modes in the process of particle acceleration.

From the analysis of the Coma field, we also conclude the following:

1. To the NE of Coma, at a projected distance of $\sim 1.2\ R_{\rm vir}$, an arc-like diffuse patch of emission is discovered. As a large-scale filament of galaxies is detected in that direction, we tentatively propose that this emission is due to particles re-accelerated by an accretion shock, and we name this emission "accretion relic." If confirmed, this would be the first detection of particle acceleration from an accretion shock.
2. The halo front, already reported by Brown & Rudnick (2011), is here confirmed coincident with the position of

a shock front detected in both X-ray and SZ studies (Planck Collaboration et al. 2013; Churazov et al. 2021). The radio spectral index does not seem to follow the typical trend found in radio relics. However, the large errors due to the small frequency range used to compute the spectral index do not allow us to exclude such a trend. It is possible that the halo front is caused by the radio halo plasma dragged along by the shock wave and compressed by it. In any case, we can conclude that the properties of the halo in the west region are affected by the shock passage.

3. The radio relic in the Coma cluster is here imaged with unprecedented detail, thanks to both the sensitivity of the LOFAR observations and the calibration techniques that we have used, which allow us to minimize the artifacts from Coma A. The relic emission is connected to the tail of NGC 4879, which is likely moving toward the SW. The connection between the relic and NGC 4879 is what we name the NAT–relic connection. The 20″ resolution image shows that the endpoints of the NGC 4879 jets are well distinct from the weak diffuse emission of the NAT–relic connection. A bright bar of radio emission is detected, similar to what has been found in other cluster tails (e.g., Clarke et al. 2013). We have discussed three possible scenarios to explain the presence of the NAT–relic connection and propose that NGC 4879 is moving supersonically toward the SW. During its motion, it has crossed the shock at the position of the relic. The shock has reenergized the particles injected by the tail in the ICM in the past and left behind during the galaxy's motion through the ICM.

Using literature information about the merging scenario of Coma and its large-scale structure environment, we can outline a global picture to explain the observed radio emission. The Coma cluster is currently accreting matter through filaments of galaxies that connect it to A1367 (Malavasi et al. 2020). A recent merger has happened between Coma and the galaxy group NGC 4839, which has passed the cluster from NE to SW, injecting a first shock wave in the ICM that is now powering the radio relic emission (Lyskova et al. 2019). The cluster core has been perturbed by this merger, and possibly from previous less massive mergers, which have released thermal energy in the ICM. A small fraction of this energy has been dissipated in turbulent motions, which have re-accelerated a mildly relativistic population of CRe already present in the ICM originating the radio halo.

From the global spectral index of the halo, its radial trend, and the analysis of the radio–X-ray correlation, we are able to derive a coherent picture where particles are re-accelerated by homogeneous turbulence in the ICM. In this picture, we have made several working assumptions that indicate possible regimes for re-acceleration to operate (i.e., constant turbulent Mach number and a radial increase of the CRe energy density with respect to the thermal energy density). We have attempted to distinguish between re-acceleration by Transit-Time-Damping with compressive modes and non-resonant second-order Fermi acceleration with solenoidal modes, and although present data are not accurate enough, we have shown that observations are entering a regime where the details of the model can be in principle tested. It is possible that future observations, either with LOFAR 2.0 and/or MeerKAT, will be able to make an additional step forward and unveil the details of turbulent re-acceleration.

The cluster core has been perturbed by the passage of NGC 4839, and its motion around its equilibrium position has caused a second shock wave (Lyskova et al. 2019; Churazov et al. 2021) whose front is now coincident with the halo front. We find that the spectrum of the halo front has been affected by the shock passage, but we are not able to distinguish between shock re-acceleration or compression by the shock wave.

NGC 4839 is now at its second passage toward the cluster center (Lyskova et al. 2019; Churazov et al. 2021). Its motion might have injected additional turbulence in the ICM and a considerable amount of seed electrons, which originate the radio bridge (Bonafede et al. 2021). The NAT galaxy NGC 4789 that is now located to the SW of the relic is moving away from the cluster center at a supersonic velocity after crossing the shock wave at the location of the relic. From this interaction, the radio plasma injected in the ICM by NGC 4789 has been reenergized, leading to the emission that we detect in the NAT–relic connection.

Finally, a filament of matter is detected to the NE of the Coma cluster. The matter accreting toward the cluster from that direction could result in the tentative "accretion relic" that we have discovered.

The scenario that we outline here is not the only possible one, and it leaves open questions. However, our analysis shows that we are entering a new era for the physics of non-thermal ICM emission, where we can constrain the model parameters.

A.B., E.B., N.B., and C.J.R. acknowledge support from the ERC Starting Grant "DRANOEL," No. 714245. A.B. and C.S. acknowledge support from the MIUR grant FARE "SMS." F.V., K.R., and M. Brienza acknowledge support from the ERC Starting Grant "MAGCOW," No. 714196. H.B. and P.M. acknowledge financial contribution from the contracts ASI-INAF Athena 2019-27-HH.0, "Attivitá di Studio per la comunità scientifica di Astrofisica delle Alte Energie e Fisica Astroparticellare" (Accordo Attuativo ASI-INAF n. 2017-14-H.0), from the European Union's Horizon 2020 Programme under the AHEAD2020 project (grant agreement No. 871158), and support from INFN through the InDark initiative. M. Brüggen acknowledges funding by the Deutsche Forschungsgemeinschaft (DFG, German Research Foundation) under Germany's Excellence StrategyEXC 2121 Quantum Universe390833306. A. Botteon acknowledges support from the VIDI research program with project No. 639.042.729, which is financed by the Netherlands Organisation for Scientific Research (NWO). R.J.v.W. acknowledges support from the ERC Starting Grant ClusterWeb 804208. X.Z. acknowledges support from Chinese Scholarship Council (CSC). A.S. is supported by the Women In Science Excel (WISE) program of the NWO. M.R. and F.G. acknowledge support from INAF mainstream project "Galaxy Clusters science with LOFAR." LOFAR, the Low Frequency Array designed and constructed by ASTRON, has facilities owned by various parties (each with their own funding sources) and that are collectively operated by the International LOFAR Telescope (ILT) foundation under a joint scientific policy. The LOFAR software and dedicated reduction packages on https://github.com/apmechev/GRID_LRT were deployed on the e-infrastructure by the LOFAR e-infragroup, consisting of J.B.R.O. (ASTRON & Leiden Observatory), A.P.M. (Leiden Observatory), and T.S. (Leiden

Observatory) with support from N. Danezi (SURFsara) and C. Schrijvers (SURFsara). This research had made use of the NASA/IPAC Extragalactic Database (NED), which is operated by the Jet Propulsion Laboratory, California Institute of Technology, under contract with the National Aeronautics and Space Administration.

Software: Ciao v4.13 (Fruscione et al. 2006), ENZO (Bryan et al. 2014; Vazza et al. 2018), Astropy (Astropy Collaboration et al. 2013, 2018) DDFacet (Tasse et al. 2018) APLpy (Robitaille & Bressert 2012), wsclean (Offringa & Smirnov 2017).

Appendix
XMM-Newton ObsIDs

The ObsIDs of the XMM-Newton observations we analyzed are 58940701, 124710101, 124710301, 124710401, 124710501, 124710601, 124710701, 124710801, 124710901, 124711101, 124711401, 124711601, 124712001, 124712101, 124712201, 124712401, 124712501, 153750101, 204040101, 204040201, 204040301, 300530101, 300530201, 300530301, 300530401, 300530501, 300530601, 300530701, 304320201, 304320301, 304320801, 403150101, 403150201, 403150301, 403150401, 652310201, 652310301, 652310401, 652310501, 652310601, 652310701, 652310801, 652310901, 652311001, 691610201, 691610301, 800580101, 800580201, 851180501, 841680101, 841680201, 841680401, 841680501, 841680301, 841680801, 841680601, and 841680701.

ORCID iDs

A. Bonafede https://orcid.org/0000-0002-5068-4581
L. Rudnick https://orcid.org/0000-0001-5636-7213
G. Giovannini https://orcid.org/0000-0003-4916-6362
T. W. Shimwell https://orcid.org/0000-0001-5648-9069
A. Simionescu https://orcid.org/0000-0002-9714-3862
M. Brüggen https://orcid.org/0000-0002-3369-7735
K. Rajpurohit https://orcid.org/0000-0001-7509-2972
C. Stuardi https://orcid.org/0000-0003-1619-3479
L. Feretti https://orcid.org/0000-0003-0312-6285
A. Botteon https://orcid.org/0000-0002-9325-1567
E. Carretti https://orcid.org/0000-0002-3973-8403
R. Cassano https://orcid.org/0000-0003-4046-0637
F. de Gasperin https://orcid.org/0000-0003-4439-2627
F. Gastaldello https://orcid.org/0000-0002-9112-0184
R. J. van Weeren https://orcid.org/0000-0002-0587-1660

References

Adami, C., Biviano, A., Durret, F., & Mazure, A. 2005, A&A, 443, 17
Akamatsu, H., Inoue, S., Sato, T., et al. 2013, PASJ, 65, 89
Astropy Collaboration, Price-Whelan, A. M., Sipőcz, B. M., et al. 2018, AJ, 156, 123
Astropy Collaboration, Robitaille, T. P., Tollerud, J., et al. 2013, A&A, 558, A33
Baldi, A. S., Bourdin, H., Mazzotta, P., et al. 2019, A&A, 630, A121
Ballarati, B., Feretti, L., Ficarra, A., et al. 1981, A&A, 100, 323
Biava, N., de Gasperin, F., Bonafede, A., et al. 2021, MNRAS, 508, 3995
Bonafede, A., Brunetti, G., Vazza, F., et al. 2021, ApJ, 907, 32
Bonafede, A., Feretti, L., Murgia, M., et al. 2010, A&A, 513, A30
Bonafede, A., Intema, H. T., Brüggen, M., et al. 2014, MNRAS, 444, L44
Bonafede, A., Vazza, F., Brüggen, M., et al. 2013, MNRAS, 433, 3208
Botteon, A., Brunetti, G., van Weeren, R. J., et al. 2020a, ApJ, 897, 93
Botteon, A., van Weeren, R. J., Brunetti, G., et al. 2020b, MNRAS, 499, L11
Boxelaar, J., van Weeren, R., & Botteon, A. 2021, A&C, 35, 100464
Botteon, A., Shimwell, T. W., Cassano, R., et al. 2022, A&A, 660, A78
Briel, U. G., Henry, J. P., Lumb, D. H., et al. 2001, A&A, 365, L60
Brown, S., & Rudnick, L. 2011, MNRAS, 412, 2
Brunetti, G., Giacintucci, S., Cassano, R., et al. 2008, Natur, 455, 944
Brunetti, G., & Jones, T. W. 2014, IJMPD, 23, 1430007
Brunetti, G., & Lazarian, A. 2007, MNRAS, 378, 245
Brunetti, G., & Lazarian, A. 2011, MNRAS, 410, 127
Brunetti, G., & Lazarian, A. 2016, MNRAS, 458, 2584
Brunetti, G., Rudnick, L., Cassano, R., et al. 2013, A&A, 558, A52
Brunetti, G., Setti, G., Feretti, L., & Giovannini, G. 2001, MNRAS, 320, 365
Brunetti, G., & Vazza, F. 2020, PhRvL, 124, 051101
Bryan, G. L., Norman, M. L., O'Shea, B. W., et al. 2014, ApJS, 211, 19
Burns, J. O., Roettiger, K., Ledlow, M., & Klypin, A. 1994, ApJL, 427, L87
Cassano, R., & Brunetti, G. 2005, MNRAS, 357, 1313
Churazov, E., Khabibullin, I., Lyskova, N., Sunyaev, R., & Bykov, A. M. 2021, A&A, 651, A41
Clarke, T. E., Randall, S. W., Sarazin, C. L., Blanton, E. L., & Giacintucci, S. 2013, ApJ, 772, 84
Condon, J. J., Cotton, W. D., Greisen, E. W., et al. 1998, AJ, 115, 1693
Cordey, R. A. 1985, MNRAS, 215, 437
Cuciti, V., Cassano, R., Brunetti, G., et al. 2015, A&A, 580, A97
Donnert, J., Dolag, K., Lesch, H., & Müller, E. 2009, MNRAS, 392, 1008
Enßlin, T. A., & Gopal-Krishna 2001, A&A, 366, 26
Feretti, L., Schuecker, P., Böhringer, H., Govoni, F., & Giovannini, G. 2005, A&A, 444, 157
Fruscione, A., McDowell, J. C., Allen, G. E., et al. 2006, Proc. SPIE, 6270, 62701V
Gastaldello, F., Ghizzardi, S., Marelli, M., et al. 2017, ExA, 44, 321
Giovannini, G., Feretti, L., & Stanghellini, C. 1991, A&A, 252, 528
Giovannini, G., Feretti, L., Venturi, T., Kim, K.-T., & Kronberg, P. P. 1993, ApJ, 406, 399
Govoni, F., Feretti, L., Giovannini, G., et al. 2001, A&A, 376, 803
Govoni, F., Orrù, E., Bonafede, A., et al. 2019, Sci, 364, 981
Hanisch, R. J., & Erickson, W. C. 1980, AJ, 85, 183
Hardcastle, M. J., Gürkan, G., van Weeren, R. J., et al. 2016, MNRAS, 462, 1910
Hoang, D. N., Brüggen, M., & Botteon, A. 2022, arXiv:2206.04666
Hoang, D. N., Zhang, X., Stuardi, C., et al. 2021, A&A, 656, A154
Hong, S. E., Ryu, D., Kang, H., & Cen, R. 2014, ApJ, 785, 133
Ignesti, A., Brunetti, G., Gitti, M., & Giacintucci, S. 2020, A&A, 640, A37
Kang, H., Ryu, D., & Jones, T. W. 2012, ApJ, 756, 97
Kelly, B. C. 2007, ApJ, 665, 1489
Kronberg, P. P., Kothes, R., Salter, C. J., & Perillat, P. 2007, ApJ, 659, 267
Large, M. I., Mathewson, D. S., & Haslam, C. G. T. 1959, Natur, 183, 1663
Lyskova, N., Churazov, E., Zhang, C., et al. 2019, MNRAS, 485, 2922
Malavasi, N., Aghanim, N., Tanimura, H., Bonjean, V., & Douspis, M. 2020, A&A, 634, A30
Marelli, M., Molendi, S., Rossetti, M., et al. 2021, ApJ, 908, 37
Markevitch, M. 2010, arXiv:1010.3660
Miniati, F., & Beresnyak, A. 2015, Natur, 523, 59
Mirakhor, M. S., & Walker, S. A. 2020, MNRAS, 497, 3204
Murgia, M., Govoni, F., Markevitch, M., et al. 2009, A&A, 499, 679
Nolting, C., Jones, T. W., O'Neill, B. J., & Mendygral, P. J. 2019, ApJ, 885, 80
Offringa, A. R., & Smirnov, O. 2017, MNRAS, 471, 301
Ogrean, G. A., & Brüggen, M. 2013, MNRAS, 433, 1701
Ogrean, G. A., Brüggen, M., van Weeren, R. J., et al. 2013, MNRAS, 433, 812
Pfrommer, C., & Enßlin, T. A. 2004, A&A, 413, 17
Pizzo, R. F. 2010, PhD Thesis, Kapteyn Institute
Planck Collaboration, Abergel, A., Ade, P. A. R., et al. 2014, A&A, 571, A11
Planck Collaboration, Ade, P. A. R., Aghanim, N., et al. 2011, A&A, 536, A8
Planck Collaboration, Ade, P. A. R., Aghanim, N., et al. 2013, A&A, 554, A140
Planck Collaboration, Akrami, Y., Ashdown, M., et al. 2020, A&A, 644, A99
Raja, R., Rahaman, M., Datta, A., et al. 2020, MNRAS, 493, L28
Rajpurohit, K., Brunetti, G., Bonafede, A., et al. 2021a, A&A, 646, A135
Rajpurohit, K., Hoeft, M., Vazza, F., et al. 2020, A&A, 636, A30
Rajpurohit, K., van Weeren, R. J., Hoeft, M., et al. 2022, ApJ, 927, 80
Rajpurohit, K., Vazza, F., van Weeren, R. J., et al. 2021b, A&A, 654, A41
Riseley, C. J., Rajpurohit, K., Loi, F., et al. 2022, MNRAS, 512, 4210
Robitaille, T., & Bressert, E. 2012, APLpy: Astronomical Plotting Library in Python, Astrophysics Source Code Library, ascl:1208.017
Rudnick, L. 2002, NewAR, 46, 101
Savini, F., Bonafede, A., Brüggen, M., et al. 2018, MNRAS, 478, 2234
Savini, F., Bonafede, A., Brüggen, M., et al. 2019, A&A, 622, A24
Shimwell, T. W., Hardcastle, M. J., Tasse, C., et al. 2022, A&A, 659, A1
Shimwell, T. W., Röttgering, H. J. A., Best, P. N., et al. 2017, A&A, 598, A104
Shimwell, T. W., Tasse, C., Hardcastle, M. J., et al. 2019, A&A, 622, A1

Simionescu, A., Werner, N., Urban, O., et al. 2013, ApJ, 775, 4
Stuardi, C., Bonafede, A., Wittor, D., et al. 2019, MNRAS, 489, 3905
Tasse, C., Hugo, B., Mirmont, M., et al. 2018, A&A, 611, A87
Thierbach, M., Klein, U., & Wielebinski, R. 2003, A&A, 397, 53
Trasatti, M., Akamatsu, H., Lovisari, L., et al. 2015, A&A, 575, A45
van Haarlem, M. P., Wise, M. W., Gunst, A. W., et al. 2013, A&A, 556, A2
van Weeren, R. J., Andrade-Santos, F., Dawson, W. A., et al. 2017, NatAs, 1, 0005
van Weeren, R. J., de Gasperin, F., Akamatsu, H., et al. 2019, SSRv, 215, 16
van Weeren, R. J., Röttgering, H. J. A., Rafferty, D. A., et al. 2012, A&A, 543, A43
Vazza, F., Brunetti, G., Brüggen, M., & Bonafede, A. 2018, MNRAS, 474, 1672
Vazza, F., Jones, T. W., Brüggen, M., et al. 2017, MNRAS, 464, 210
Vazza, F., Locatelli, N., Rajpurohit, K., et al. 2021, Galax, 9, 109
Venturi, T., Giacintucci, S., Merluzzi, P., et al. 2022, A&A, 660, A81
Venturi, T., Giovannini, G., & Feretti, L. 1990, AJ, 99, 1381
Venturi, T., Rossetti, M., Brunetti, G., et al. 2017, A&A, 603, A125
Wilber, A., Brüggen, M., Bonafede, A., et al. 2018, MNRAS, 473, 3536
Zhang, C., Churazov, E., & Zhuravleva, I. 2021, MNRAS, 501, 1038
Zhang, X., Simionescu, A., Akamatsu, H., et al. 2020, A&A, 642, A89
ZuHone, J. A., Markevitch, M., Brunetti, G., & Giacintucci, S. 2013, ApJ, 762, 78